Ordered ring-shaped cracks induced by indentation in metal films on soft elastic substrates

Senjiang Yu,[1,*] Long Ma,[2,*] Linghui He,[2] Lingwei Li,[1,†] and Yong Ni[2,‡]

[1]*Institute of Advanced Magnetic Materials, College of Materials and Environmental Engineering, Hangzhou Dianzi University, Hangzhou 310018, People's Republic of China*

[2]*CAS Key Laboratory of Mechanical Behavior and Design of Materials, Department of Modern Mechanics, University of Science and Technology of China, Hefei, Anhui 230026, People's Republic of China*

(Received 1 May 2020; accepted 14 July 2020; published 3 August 2020)

Ordered crack patterns contain plentiful physical mechanisms and are useful for technological applications such as lithography, template, and biomimicry. Here we report on ordered multiple ring-shaped cracks induced by indentation in metal films on soft elastic polydimethylsiloxane (PDMS) substrates. It is shown that the indentation triggers the deformation of PDMS substrate and generates a radial tensile stress in the film, leading to the formation of ring-shaped cracks with a nearly uniform spacing. The morphological characteristics and evolution behaviors of the multiple ring-shaped cracks are revealed by optical microscopy, atomic force microscopy, and scanning electron microscopy. Their formation mechanisms are discussed by theoretical analysis based on the fracture mechanics. The report in this work can promote better understanding of the indentation-induced stress anisotropy and mode competition in rigid-film–soft-substrate systems and provide a facile strategy to control the crack patterns by simple mechanical loading.

DOI: 10.1103/PhysRevE.102.022801

I. INTRODUCTION

Fracture patterns are very common in natural and artificial systems that span a wide range of scales, from macroscopic planet surfaces, rocks, drying mud, aged paints, coatings, and crocodile skins to microscopic films, graphene layers, nanotubes, and core-shell structures [1–3]. They are generated by residual tensile stresses which originate from various factors including weathering, desiccation, heating and cooling, mechanical loading, and electrical, optical, and chemical stimuli. The crack morphologies are strongly dependent on the tensile stress field in the material. The most common crack mode observed in homogeneous materials (especially the film-substrate bilayer systems) is a disordered crack network composed of a large number of straight crack segments because the tensile stress is isotropic or equal biaxially [1,2]. The adjacent straight cracks in the network usually connect perpendicularly with each other (90° junctions). Studies have shown that an ordered hexagonal crack network (120° junctions) can form by repeated open and close cycles of cracks [4]. In addition, other regular crack patterns can spontaneously form occasionally in film-substrate systems. For example, gradual desiccation of a suspension can induce a twisting stress field due to the normal and radial humidity gradients in the precipitate fragment and result in spiral cracks [5,6]. Due to the collaborative effect of delamination and fracture, the cracks can self-replicate to form crescent alleys, spirals, or long bands in sol-gel films, depending on the geometry of the initiation spot [7,8].

Although fracture is usually considered a nuisance in various manufacturing processes, increasing attention has been given recently to control it and use cracks as a facile low-cost strategy for producing highly ordered structures at micro and nano length scales [9–15]. Controllable crack patterns can be useful in a wide range of applications including controllable patterning [9,10], controlled wettability [11], stretchable transistors [12], ultrasensitive sensors [13], biological assays [14], micro- and nanofluidic devices [15], etc.

At present, various strategies have been developed to manipulate the stress field in the material and thus to control the crack orientation and dimension. Yuse and Sano reported that straight, oscillating and branched cracks can form on a quenched glass specimen and the morphologies are dependent on the temperature difference between the hot and cold reservoirs and the sample descending speed [16]. Stretching or bending a brittle film in one direction can generate uniaxial tensile stress and parallel cracks aligned perndicular to the loading direction [15,17]. However, the crack positions are usually random and the spacings are not uniform for this technique. Kim *et al.* prefabricated triangular notch structures to accurately control the crack position and density [18]. Then the same group fabricated bidirectional crack patterns by using diamond-shaped notch structures and biaxial stretching in sequence [19]. The previous studies showed that the cracks in glassy films could penetrate deep into crystallized substrates, resulting in the linear oscillating propagation of cracks along specific orientations [9,20]. Alaca *et al.* employed a sharp notch and open boundary trench to locally regulate the tensile stress in SiO_2 films and control crack initiation and termination at predetermined positions [21]. Kim *et al.* produced multidirectional crack patterns by using notches with different configurations and a single- or double-photomask process [22]. Several groups observed microscale wavy cracks

*These authors contributed equally to this work.
†lingwei@hdu.edu.cn
‡yni@ustc.edu.cn

in brittle films on patterned metal, polymer, grapheme, and liquid stripes [23,24]. Mitchell *et al.* reported that the substrate curvature could stimulate or suppress the growth of cracks and regulate the crack paths [25].

In this work we report on the spontaneous formation of ordered ring-shaped cracks induced by indentation in metal films deposited on soft elastic polydimethylsiloxane (PDMS) substrates. The indentation can trigger the deformation of the PDMS substrate and generates a radial tensile stress in the film, resulting in the formation of multiple ring-shaped cracks with a nearly uniform spacing. The morphological characteristic, evolutional behavior, and formation mechanism of such crack pattern are investigated by experiment and theoretical analysis. The results provide the ability to generate highly ordered ring-shaped cracks via regulating the film thickness and mechanical loading.

II. EXPERIMENTAL DETAILS

A. Soft-substrate fabrication

We adopted polydimethylsiloxane (Dow Corning Sylgard 184 silicone rubber) as the soft elastic substrates. The prepolymers and cross-linkers were mixed with a 10:1 weight ratio. After degassing in a low-pressure chamber (several hundred pascals), the liquid PDMS was spin coated onto clean glass slides $\sim 10 \times 10\,\mathrm{mm}^2$ in size. Then the samples were baked at 80 °C above 3 h to cross-link the mixture completely. After curing, the thickness of the PDMS layer was about 20 μm and the elastic modulus of PDMS was ~ 1.7 MPa.

B. Film deposition

Metal films were deposited on the PDMS substrates by direct current magnetron sputtering technique at room temperature. The target was a purified chromium disk with 60 mm in diameter and 3 mm in thickness. Note that the film material is not restricted to chromium. Similar ring-shaped cracks can be observed in a variety of metal materials including silver, copper, nickel, tantalum, iron, tungsten, zinc, cobalt, and titanium, as shown in Fig. S1 of the Supplemental Material [26]. The deposition rate of chromium film was about 10 nm/min. The deposition time, controlled precisely by a computer, ranged from 1 to 40 min.

C. Indentation loading

After deposition, the indentation tests were performed by using a Vickers diamond indenter (HXS-1000AY). The peak load P ranged from 0.1 to 10 N. The loading rate and holding time were fixed at 0.5 N/s and 30 s, respectively. Our experiment showed that the loading conditions had no obvious influence on the crack morphologies. To obtain more structural information and extend the load range, a Berkovich nanoindenter (Agilent, G200) was also used in the experiment. The peak load P ranged from 0.5 to 500 mN. The load-depth curves were automatically recorded during nanoindentation.

D. Characterization

The surface morphologies of the samples were taken by optical microscopy (Olympus BX41) and scanning electron microscopy (SEM) (Zeiss Supra 55). The three-dimensional (3D) structures were scanned by an atomic force microscopy (AFM) (XE-100E, PSIA) operated in noncontact mode. The maximum scanning area of the AFM was $45 \times 45\,\mu\mathrm{m}^2$.

III. RESULTS AND DISCUSSION

A. Indenter-induced cracks

Figure 1(a) shows the overview of the chromium film with $h = 30$ nm triggered by the indentation with the peak load P ranging from 0.1 to 10 N. Figure 1(b) shows the enlarged views of the indentation-induced structures for $P = 0.1$, 1, and 10 N. The SEM images of the indentation-induced structures at different positions for $P = 10$ N are shown in Fig. S2 in the Supplemental Material [26]. We find that the indentation destroys the film greatly, especially near the indentation center. Radial and ring-shaped cracks can be seen clearly. The radial cracks are disorderly distributed, while the ring-shaped cracks are regularly arranged and possess a uniform spacing. Although the *in situ* growths of the radial and ring-shaped cracks under the indentation process are unavailable in our experiment, their formations can be achieved by comparing the morphologies under different peak loads. It is clear that the radial and ring-shaped cracks start to form at the indentation center. Then they propagate outward gradually as the load increases. Interestingly, the ring-shaped cracks form one by one with a uniform spacing during the indentation process.

To detect more structural details of the indentation-induced cracks, they were taken by AFM and the 2D images are shown in Fig. 2. The 3D AFM images and enlarged 2D images are shown in Figs. S3 and S4 of the Supplemental Material [26]. Figure 3(a) shows a comparison of the profiles for varying peak loads. Figure 3(b) shows the enlarged view of the profile line for $P = 10$ N. It is interesting that the film surfaces are lifted up obviously near the cracks (both radial and ring-shaped cracks), showing buckled or wrinkled structures. We suggest that the buckling phenomenon is mainly due to the residual compressive stress in the film, which originates from the nonequilibrium growth of the film and the thermal mismatch between the film and PDMS substrate [27]. The residual compressive stress in chromium films is generally smaller than the critical stress for spontaneous wrinkle formation and thus the film surfaces are frequently unwrinkled before indentation.

After the cracks form during the indentation process, the residual compressive stress is susceptible to concentrating at the crack edge, resulting in the appearance of buckled or wrinkled structures [28,29]. As shown in Figs. 3(a) and 3(b), each buckle has a sharp crease at the ridge which corresponds to the crack in the film. Such buckle profiles are quite different from the periodic wrinkles with sinusoidal profiles [27], but are very similar to the buckle delamination with ridge cracking [28,30]. Figures 3(c) and 3(d) show that both the buckle width and height increase slightly with increasing peak load. The buckle dimensions should be closely related to the compressive stress value. For the same film, the residual compressive stress is uniform, leading to the same buckle profile. The variation of the buckle width and height shown in Figs. 3(c) and 3(d) results from the indentation process. After indentation,

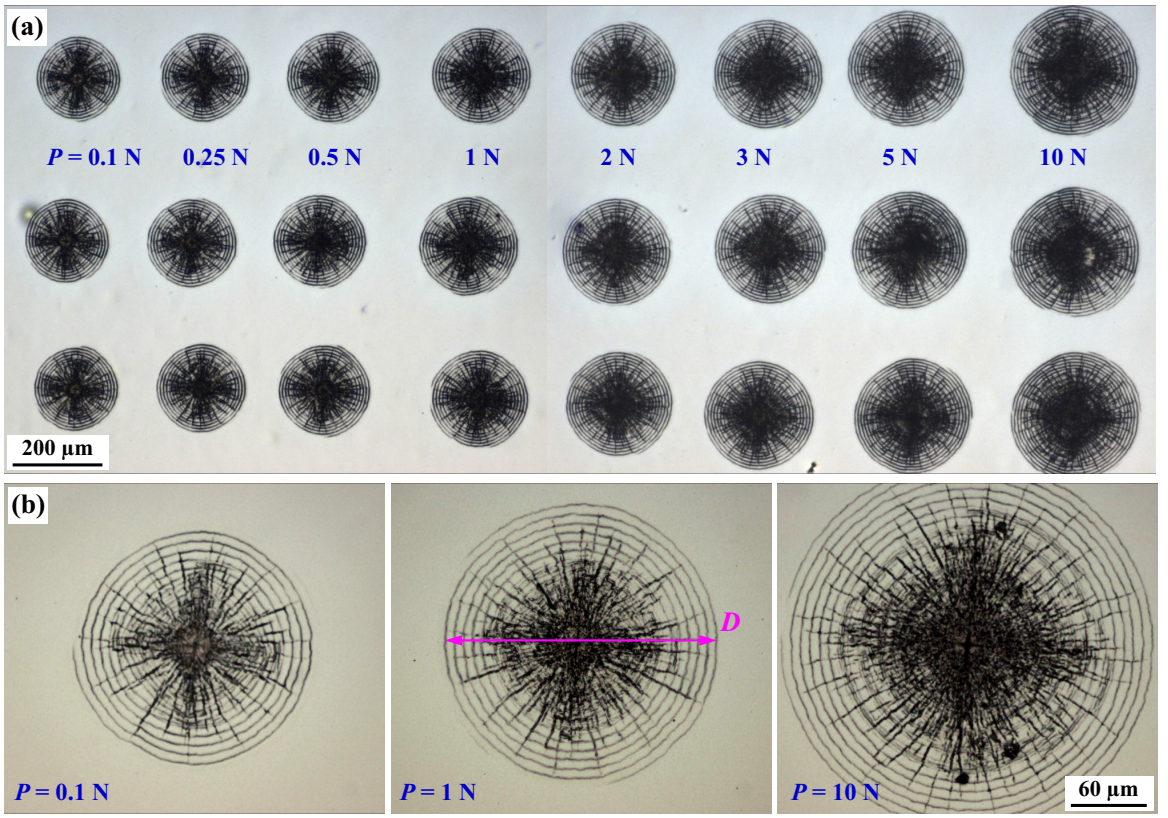

FIG. 1. (a) Overview of the indentation-induced morphologies in a chromium film deposited on the PDMS substrate. The peak loads from left to right are 0.1, 0.25, 0.5, 1, 2, 3, 5, and 10 N, respectively. Three indentation-induced crack patterns for each peak load are presented for reproducibility. The film thickness is $h = 30$ nm. (b) Enlarged views of the indentation-induced structures for $P = 0.1$, 1, and 10 N (from left to right). The maximum ring diameter is denoted by D. All optical images have the same size of $300\times260\ \mu m^2$.

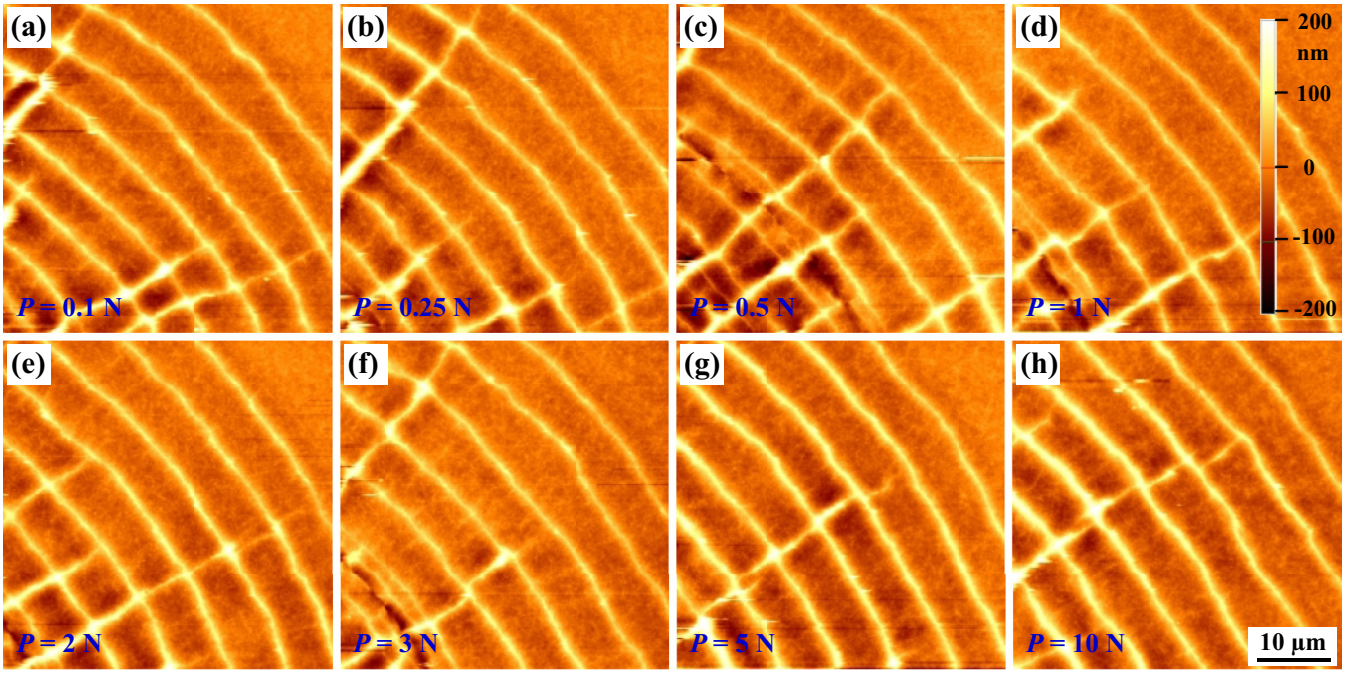

FIG. 2. Two-dimensional AFM images of the ring-shaped cracks triggered by the indentation with varying peak load shown in the bottom left corners. All images have the same size of $45\times45\ \mu m^2$. The scale bar in (d) can be applied to all the AFM images. Here $h = 30$ nm.

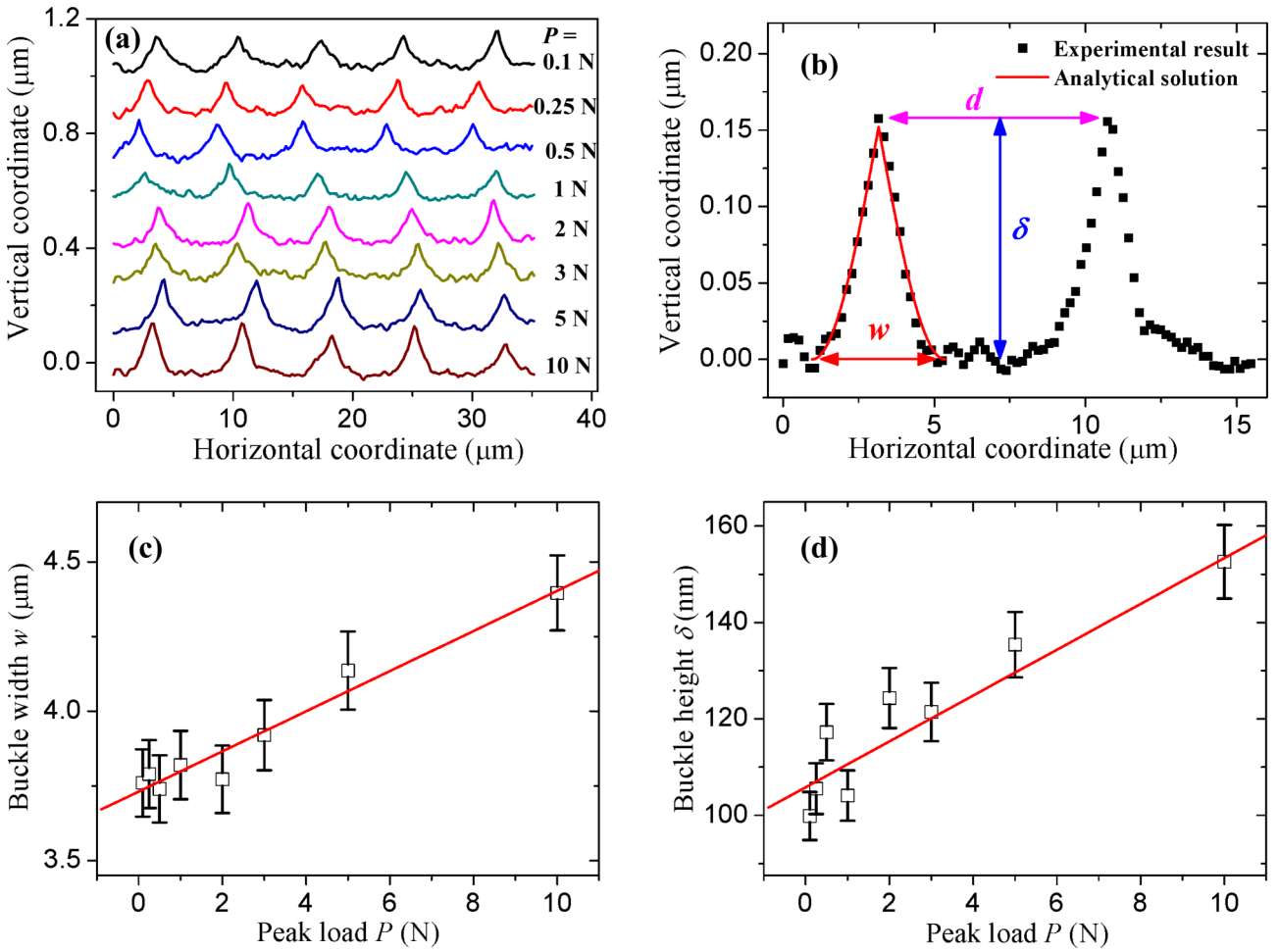

FIG. 3. (a) Comparison of the film profiles triggered by the indentation with varying peak load. (b) Enlarged view of the profile line for $P = 10$ N. The black squares are the experimental measurements while the red solid line is the analytical solution of the buckle height. The crack spacing is denoted by d. (c), (d) Dependences of the buckle width w and height δ on the peak load P. The solid lines are linear fits to the experimental data. Here $h = 30$ nm.

the PDMS substrate can be partially recovered to its original shape (elastic part), and thus an additional compression is generated in the film due to the elastic deformation of the substrate. It is clear that the additional compression increases with increasing elastic deformation (or load). Therefore, the buckle width and height increase with increasing peak load.

Figure 4 shows the morphological evolution of the ring-shaped cracks with increasing film thickness taken by optical microscopy ($P = 10$ N). Figures 5(a)–5(f) show the 2D AFM images and corresponding profiles with varying film thicknesses. The detailed morphologies of the indentation-induced cracks for different peak loads and film thicknesses are shown in Fig. S5 of the Supplemental Material [26]. We find that for the thinnest film in our experiment ($h = 10$ nm), the radial cracks are prominent while the ring-shaped cracks are comparatively sparse. The ring-shaped cracks usually terminate at some positions and their spacings are not uniform for this sample [see Fig. 5(a)]. It seems that many ring-shaped cracks have not been triggered by the largest load used in our experiment ($P = 10$ N). In the range of $h = 20-40$ nm, the films form regular ring-shaped cracks. As the film thickness further increases, the ring-shaped cracks become irregular gradually and the crack number decreases greatly. Furthermore, the buckles near the ring-shaped cracks also become irregular and their width and height are immeasurable for thicker film samples. In the range of $h = 10-60$ nm, the buckle height increases approximately linearly with the film thickness, as shown in Fig. 5(g). The increase of the buckle dimension is mainly due to the increase of the residual compressive stress and decrease of the buckle number for thicker films.

Figure 4 also shows that a cross damage zone can be seen clearly at the indentation center if the film thickness is small ($h < 60$ nm). The cross damage zone is the remaining trace of the Vickers diamond indenter used in our experiment. When the film thickness is beyond 60 nm, however, the cross damage zone becomes indistinguishable. On the other hand, the radial cracks are usually limited in the region of the maximum ring-shaped crack if the film thickness is small. As $h \geqslant 60$ nm, however, several radial cracks can propagate outward far beyond the maximum crack ring (see Fig. S5 in the Supplemental Material [26]). These radial cracks originate from the sharp edges of diamond indenter, similar to the crack phenomena induced by sharp notches in previous studies [9,18–22]. We suggest that the dense radial cracks within

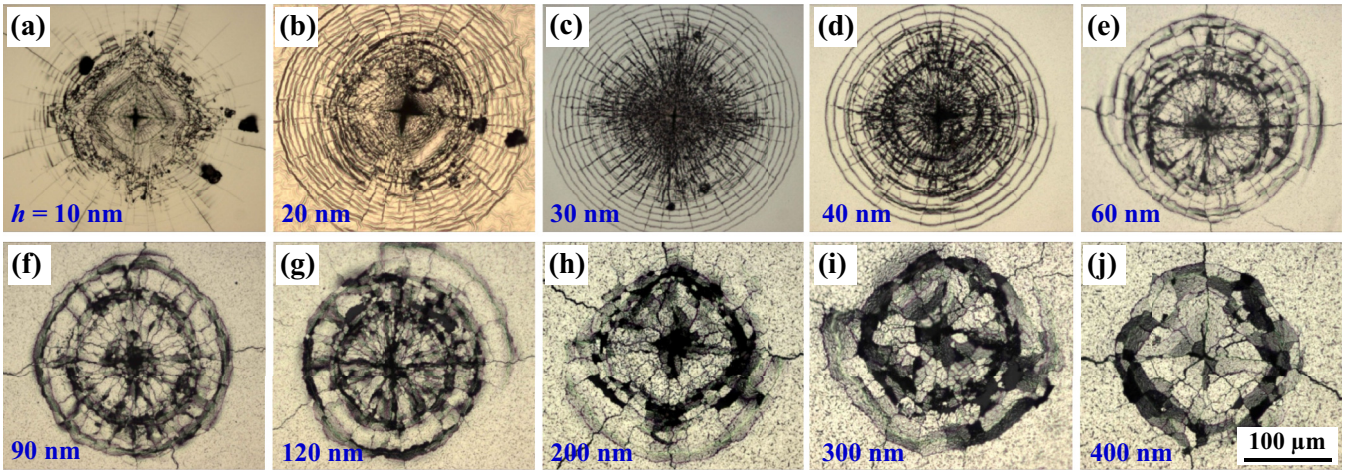

FIG. 4. Evolution of the indentation-induced cracking morphologies with the film thickness taken by optical microscopy. The data appearing in the bottom left corners represent the film thickness h. All images have the same size of $300\times260\ \mu m^2$. The peak load is $P = 10$ N.

the maximum crack ring originate from the deformation of PDMS substrate, whereas the orthogonal cracks far beyond the crack ring are caused by the film deformation itself. As the film thickness (or stiffness) increases, the stress transfer effect becomes strong. The tension caused by the indentation (especially for the four edges of the diamond indenter) can be easily transferred outward via thicker film layers, leading to the appearance of the orthogonal cracks far away from the indentation cave.

In order to further understand the structural characteristics of the ring-shaped cracks, we measured the maximum ring diameter D and crack spacing d for different peak loads and film thicknesses, as shown in Fig. 6. Overall, the maximum ring diameter increases with increasing peak load, roughly following an exponential law $D \propto \log_{10} P$ [see Fig. 6(a)]. The maximum ring diameter is weakly related to the film thickness. Figure 6(b) shows the quantitative relation between D and h for the fixed peak load ($P = 10$ N). We find that as

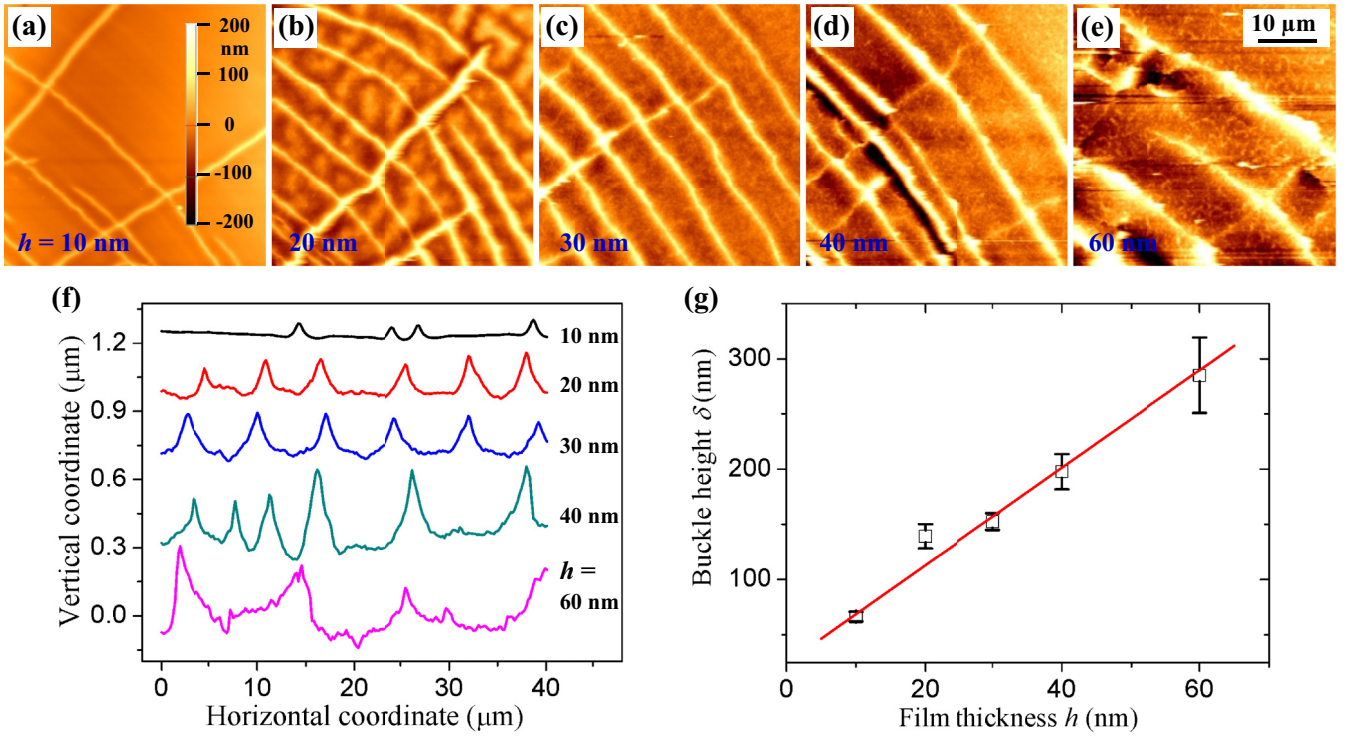

FIG. 5. (a)–(e) Two-dimensional AFM images of the indentation-induced structures in the films with varying thickness ($P = 10$ N). All images have the same size of $45\times45\ \mu m^2$. The scale bar in (a) can be applied to all the AFM images. (f) Comparison of the profiles in the films with varying thickness. (g) Dependence of the buckle height δ on the film thickness h. The solid line is a linear fit to the experimental data.

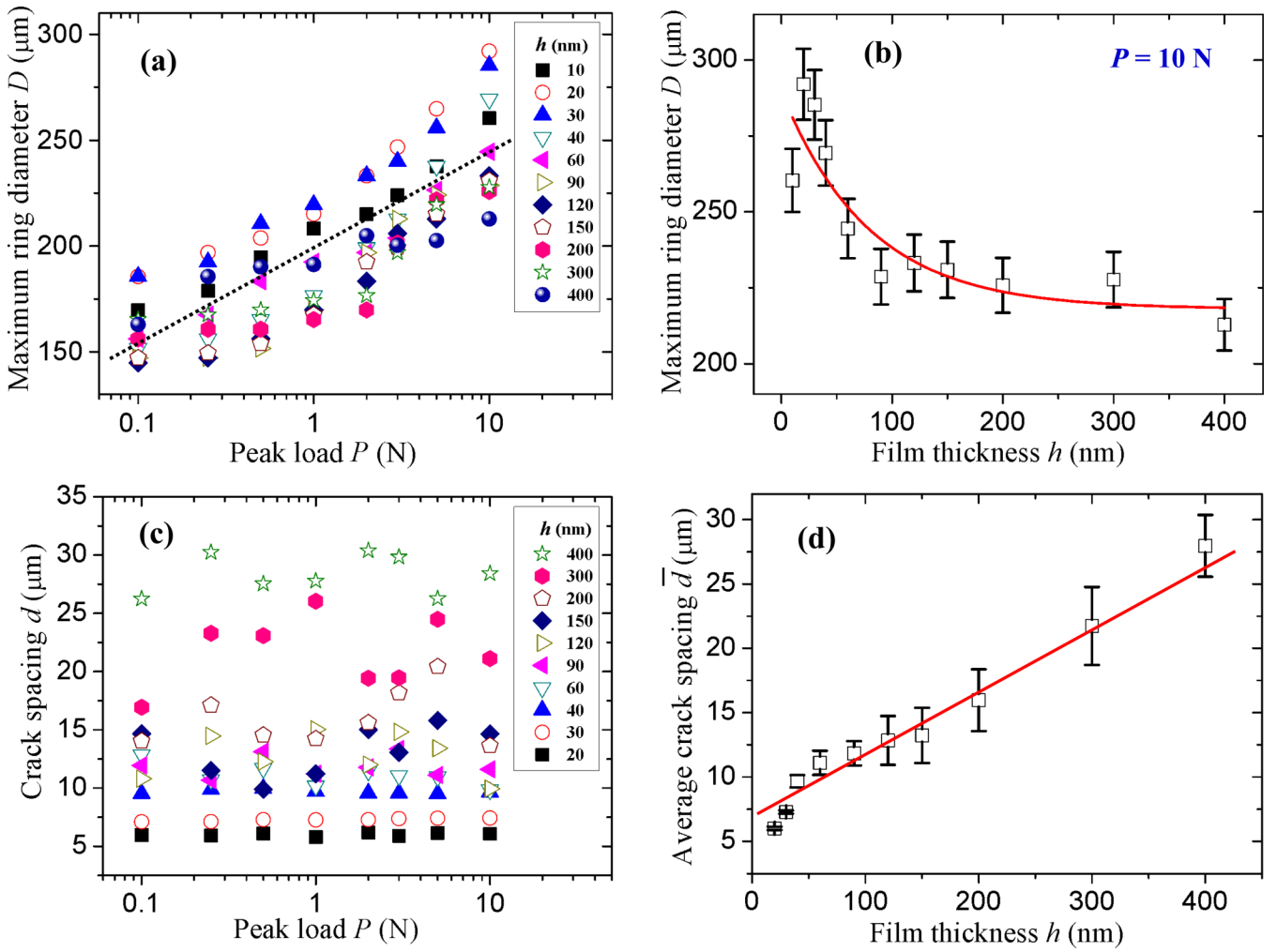

FIG. 6. (a) Dependence of the maximum ring diameter D on the peak load P for varying film thickness. The dashed line shows a linear trend for the experimental data. (b) Dependence of the maximum ring diameter D on the film thickness h with $P = 10$ N. The solid line is a guide to the eye. (c) Dependence of the crack spacing d on the peak load P for varying film thickness. (d) Dependence of the average crack spacing $\bar{d}$ on the film thickness h. The solid line is a linear fit to the experimental data.

the film thickness increases, the maximum ring diameter decreases first quickly and then slowly and finally it approaches a stable value of about 220 μm. The decrease of the maximum ring diameter for the sample with $h = 10$ nm is mainly due to the absence of larger ring-shaped cracks. Considering the radial cracks are generally located in the maximum crack ring for thinner films, the maximum ring diameter for $h = 10$ nm should be larger than that for $h = 20$ nm (see Fig. S5 in the Supplemental Material [26]).

Figure 6(c) shows the dependence of the spacing of ring-shaped cracks d on the peak load P for varying film thicknesses. The crack spacing is uniform when the film thickness is below 60 nm. For thicker films, however, the ring-shaped cracks become irregular. Although there are some fluctuations for thicker films, the crack spacing is almost independent of the peak load for all the samples. On the other hand, the crack spacing is strongly related to the film thickness. The quantitative relation between the average crack spacing $\bar{d}$ and the film thickness h is shown in Fig. 6(d). We find that the average spacing increases approximately linearly with the film thickness.

B. Nanoindenter-induced cracks

The indentation tester used above possesses a peak load ranging from 0.1 to 10 N. A peak load smaller than 0.1 N is beyond the measurement range of this tester. Furthermore, the depth information and load-displacement relation are also unavailable for this traditional indenter. To obtain more mechanical information and extend the load range, a nanoindenter was used to perform the indentation test. The nanoindenter-induced surface morphologies are shown in Fig. 7. Note that the nanoindenter (Berkovich indenter) [31] is triangle shaped while the traditional indenter (Vickers indenter) [32] is diamond shaped in the film plane. We selected seven peak loads ranging from 0.5 to 500 mN. There are two peak loads (100 and 500 mN) overlapping in the indentation and nanoindentation tests. It can be seen from Fig. 7(a) that similar ring-shaped cracks are triggered by the nanoindentation with larger peak loads. The different indenter shapes result in the same ring-shaped cracks, exhibiting the robustness of the crack patterns induced by indentation loading. The ring-shaped cracks are sparse for the nanoindenter compared to the traditional indenter with the same peak load, which may be due to the

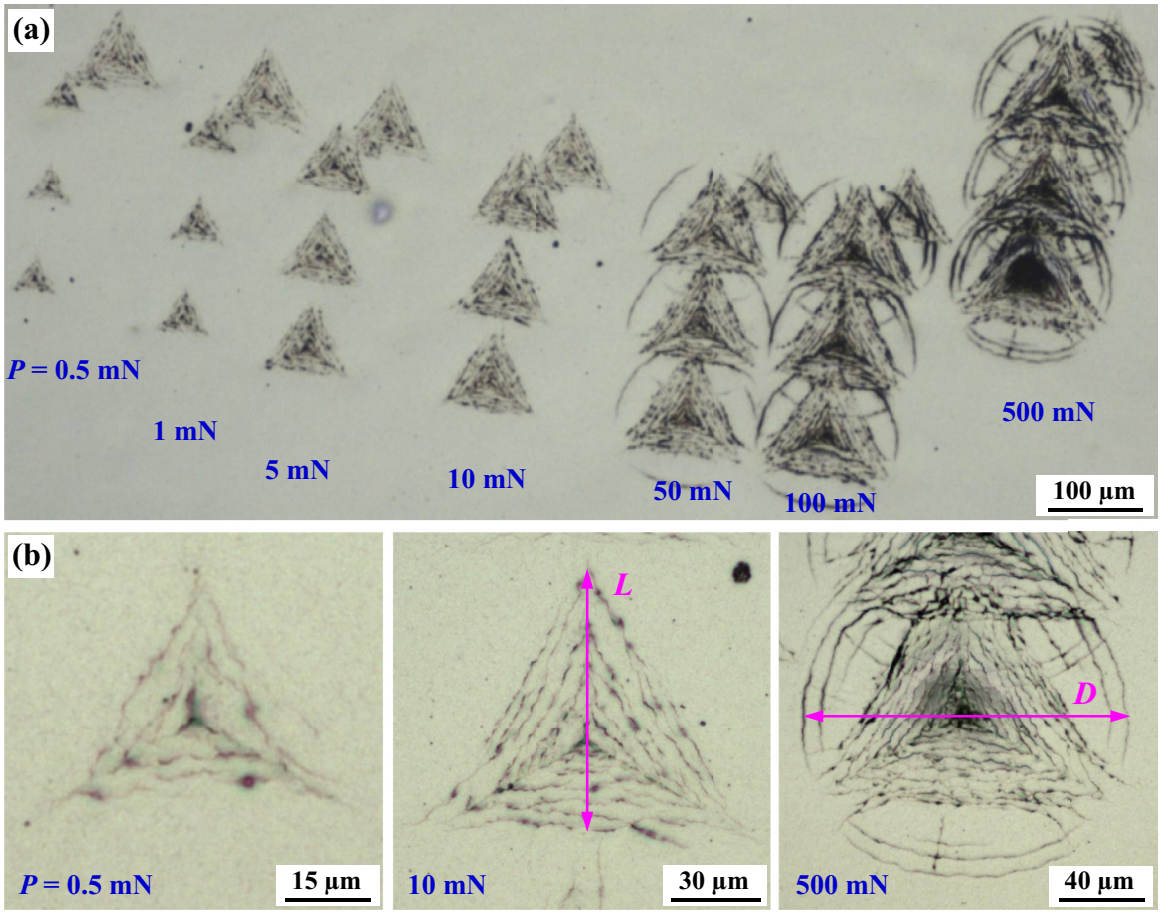

FIG. 7. (a) Overview of the crack morphologies triggered by the nanoindenter with varying peak load. (b) Enlarged views of the cracks for $P = 0.5$, 10, and 500 mN (from left to right). The triangular damage zone size is denoted by L. Here $h = 30$ nm.

different indenter shapes and operating principles. For a peak load smaller than 50 mN, the ring-shaped cracks disappear and only triangular damage zones remain. The enlarged views show that the triangular damage zone is composed of many parallel straight cracks along three different directions with 60° angles between them [see Fig. 7(b)]. These cracks do not propagate along the radial direction or peripheral direction, different from the crack patterns triggered by the traditional indenter as shown in Fig. 1.

The load-depth relations for different peak loads are shown in Fig. 8(a). The enlarged views of the load-depth curves are shown in Fig. S6 in the Supplemental Material [26]. We find that all the loading and unloading curves are very smooth and no pop-in (or sliding pop-in) structure can be seen clearly [33,34]. To further understand the influence of the load on the cracking behavior, we measured the maximum ring diameter D, triangular damage zone size L (defined as the perpendicular distance from an indenter edge to the opposite side in the film plane), and maximum depth Δ for varying peak loads in the nanoindentation test; the results are shown in Figs. 8(b) and 8(c). For comparison, the maximum ring diameters for the traditional indenter are also shown in Fig. 8(b). We find that the maximum ring diameter for the nanoindenter is somewhat smaller than that for the traditional indenter, perhaps due to the different indenter shapes and operating principles. The maximum ring diameters (both for the traditional indenter and the nanoindenter) and triangular damage zone size all increase linearly with the logarithm of the peak load, which can be expressed as $D \propto \log_{10} P$. The linear slopes of these parameters are almost identical, indicating that they obey the same evolution behavior. Figure 8(c) shows that the maximum depth also increases linearly with the logarithm of the peak load. The relationship between the damage zone dimension and the maximum depth is thus plotted in Fig. 8(d). We find that the triangular damage zone size L increases linearly with the maximum depth Δ. The maximum ring diameter D, somewhat larger than the triangular damage zone size, also increases linearly with Δ, possessing the same slope as L.

C. Formation mechanism

Fracture patterns are ubiquitous in natural and artificial systems such as tectonic plates, rocks, drying mud, aged paints, coatings, and sol-gel films. It is well known that the crack morphologies are mainly determined by the tensile stress field in the material. Disordered crack networks are frequently observed in drying mud, aged paints, coatings, and films due to the isotropic stress field [1,2]. Regular crack patterns can be achieved by tuning the stress anisotropy. The manipulating methods include uniaxial loading [15,17,18], sequent bidirectional stretching [19], directional drying [35], temperature gradient [16], boundary effect [23,24,36],

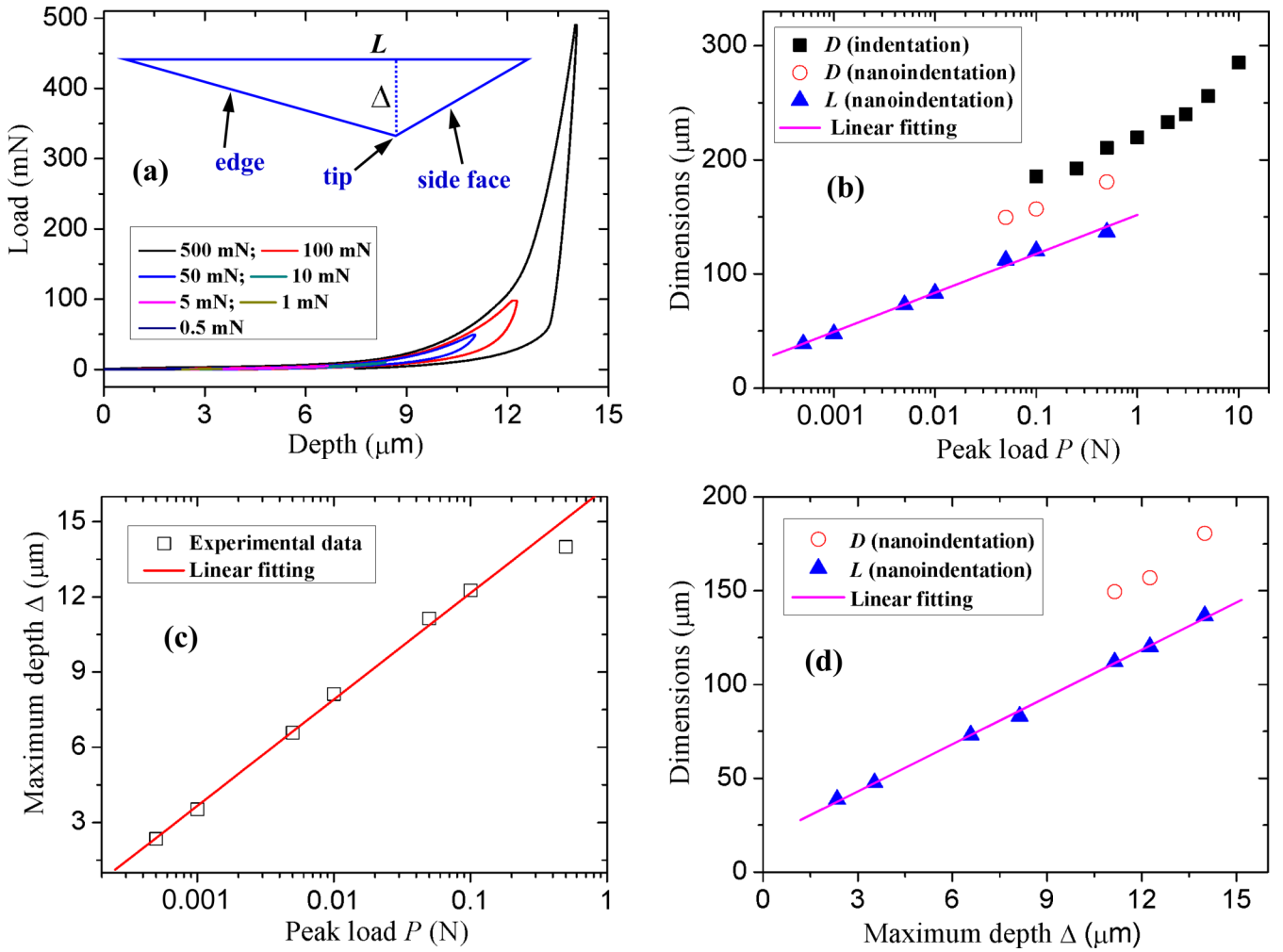

FIG. 8. (a) Load-displacement relations for different peak loads obtained from the nanoindentation. The inset shows the schematic diagram of the indenter profile. (b) Dependences of the maximum ring diameter D and triangular damage zone size L on the peak load P. (c) Dependence of the maximum depth Δ on the peak load P. (d) Dependences of the maximum ring diameter D and triangular damage zone size L on the maximum depth Δ. The solid lines in (b)–(d) are linear fits to the experimental data. Here $h = 30$ nm.

single-crystal substrate [9,20], uneven substrate surface [25], prefabricated notch array [18,19,21,22], electric-field induction [37], magnetic-field driving [38], etc.

In our experiment, the indentation (or nanoindentation) induces the stress anisotropy near the center point, leading to the formation of ordered cracks. Both the diamond-shaped indenter and triangle-shaped nanoindenter can trigger perfect ring cracks (Figs. 1 and 7), indicating that the indenter shape has no obvious influence on the ring-shaped cracks. On the other hand, the triangular damage zone in nanoindentation is highly consistent with the indenter shape in the film plane. We thus conclude that the ring-shaped cracks originate from the deformation of the PDMS substrate while the parallel straight cracks in the triangular damage zone are caused by the contact damage. Figure 7 shows that the formation of straight cracks is earlier than that of ring-shaped cracks. During the nanoindentation test, the film at the contact line is susceptible to fracture forming a straight crack. The fact that the parallel cracks have a nearly uniform spacing indicates that the crack formation is step by step during the nanoindentation process. The formation process of the parallel straight cracks is quite similar to that of the ring-shaped cracks, although their damage mechanisms are different. Because the indenter shapes in the horizontal plane at different depths are self-similar [see the inset of Fig. 8(a)], their size (i.e., the triangular damage zone size) should be directly proportional to the indentation depth, as shown in Fig. 8(d). The deviation of the fitting line from the coordinate origin is mainly due to the rounded shape at the indenter tip, leading to the decrease of the indentation depth.

The ring-shaped cracks originate from the deformation of the PDMS substrate since they are away from the indenter and the film is not in contact with the indenter directly during the crack formation. The previous theoretical analysis showed that the indenter could induce the deformation of the film-substrate system, generating a radial tensile stress in the film [33,39]. The peak radial stress always occurs outside the contact zone of the indenter. When the radial tension is beyond a critical value, i.e., the breaking strength of the film, a ring-shaped crack forms in the film some distance away from the contact zone of the indenter. The preexisting crack can effectively release the tensile stress nearby. As a

result, the radial tension in the film near the preexisting crack decreases to below the critical value and no crack forms. As the load increases, the contact zone of the indenter propagates outward and the peak radial stress increases gradually. When the peak stress is above the breaking strength of the film again, a new ring-shaped crack forms. As this process goes on, multiple ring-shaped cracks with a uniform spacing appear. The crack spacing is determined by the competition between the peak radial stress and the breaking strength of the film. It is clear that the breaking strength of the film increases with the film thickness, while the indentation-induced radial tension is almost uniform under the same load. To trigger a ring-shaped crack in thicker films, a higher tension is needed, leading to the increase of the crack spacing, as shown in Fig. 6(d). On the other hand, higher breaking strengths for thicker films suppress the formation of outermost ring-shaped cracks. Therefore the maximum ring diameter D decreases steadily with increasing film thickness h, as shown in Fig. 6(b).

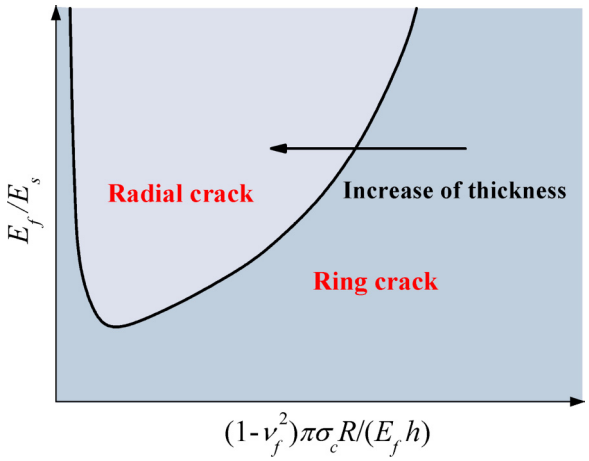

FIG. 9. Schematic diagram of the crack pattern for a film-substrate system in terms of two nondimensional parameters E_f/E_s and $\pi\sigma_c R/\bar{E}_f h$ with $\bar{E}_f = E_f/(1-\upsilon_f^2)$.

D. Theoretical analysis

It can be seen from Fig. 4 that the dominant crack modes tend to transit from rings to spokes with the increase of film thickness. According to the fracture model [39], a crack occurs when the maximum principle tensile stress is beyond the tensile strength of the film. The indenter generates an inhomogeneous stress field and previous research has shown that the maximum principal tensile stress takes place either on the surface of film along the radial direction or at the film-substrate interface along the circumferential direction [39]. The crack pattern depends on that in which direction stress reaches the tensile strength of the film first. The former case leads to ring-shaped cracks while the latter leads to radial cracks. The theoretical analysis [39] under the assumption of infinite substrate thickness shows that under a rigid spherical indenter with radius R there exist two nondimensional parameters affecting the crack pattern for the film-substrate system, E_f/E_s and $\pi\sigma_c R/\bar{E}_f h$, with $\bar{E}_f = E_f/(1-\upsilon_f^2)$, where E_f and E_s are Young's modulus of the film and substrate, and h, σ_c, and ν_f are the thickness, the fracture tensile strength, and the Poisson's ratio of the film, respectively. In our work, on one hand, except film thicknesses of 300 and 400 nm, the thickness of the substrate is 100–2000 times larger than the film thickness. In addition, the estimated radius R of the equivalent sphere indenter is also much larger than the film thickness and reduces the effect of substrate thickness [40]. On the other hand, the enormous modulus difference between the film and substrate also weakens the impact of substrate thickness on the stress field in the film. Thus the influence of substrate thickness on the crack pattern can be neglected in our work. Figure 9 shows the schematic diagram of the crack pattern depending on these two parameters. In a theoretical analysis [39] it was found that there are two possible positions of the maximum principal stress for stressed film: at the film surface and at the interface between the film and substrate along the axis of symmetry. When the maximum stress occurs at the film surface first, a ring crack would happen. Otherwise, a radial crack would appear first.

In our experiments, the Young's moduli of Cr film and PDMS substrate are about $E_f \sim 250$ GPa and $E_s \sim 1.7$ MPa, respectively. The tensile strength and the Poisson's ratio of Cr film are about $\sigma_c \sim 280$ MPa and $\nu_f = 0.21$, respectively. Although a Vickers diamond indenter is used in our experiments, due to the substrate's flexibility, the effective contact area is much larger than the indenter's size. From Fig. 4 one can see that there is a sunken area with diameter about 100 μm in the center of indentation, so the estimated radius R of the equivalent sphere indenter is larger than 100 μm.

For film thickness $h = 400$ nm, the horizontal coordinate is $\pi\sigma_c R/\bar{E}_f h \approx 0.84$; this case is located in the radial crack regime in Fig. S7 in the Supplemental Material [26] for modulus mismatch $E_f/E_s \approx 1.47\times10^5$ in our work. For the case of film thickness $h = 20$ nm, the horizontal coordinate is $\pi\sigma_c R/\bar{E}_f h \approx 16.82$. Here we use a fifth-order polynomial fitting method to obtain the curve in the phase diagram of Fig. S8 in the Supplemental Material [26] on the right of the critical modulus mismatch point. The fitting result as shown in Fig. S8 indicates that when $\pi\sigma_c R/\bar{E}_f h \approx 16.82$, the corresponding modulus mismatch is $(E_f/E_s)_c \approx 1.58\times10^7$, which is much larger than the material mismatch $E_f/E_s \approx 1.47\times10^5$ in our experiment. The result means that this case is in the lower right of the curve in the phase diagram, namely, when the film thickness $h = 20$ nm, the crack pattern is located in the ring crack regime. Thus, with the decrease of film thickness, the black arrow in Fig. 9 indicates the transition of the crack pattern regime from a ring crack toward a radial crack, which is in agreement with the experimental results shown in Fig. 4. It is worth noting that with the fitting result, the critical transition thickness is obtained as $h_c \approx 50$ nm, which is approximated to the experimental result $h_c \approx 60$ nm in Fig. 4.

The crack in the film generates a shear stress concentration zone perpendicular to the crack edge at the interface of film and substrate. If the interface is weak, there is a collaborative fracture of the crack and delamination in the film. A Griffith-criterion-based analysis [8] has shown that the collaborative fracture mode involves the combined energy release of residual elastic energy and adhesion energy and it concludes that for the patterned crack the spacing width of ad-

jacent cracks d is proportional to the film thickness h: $d \propto h$. The experimental result in Fig. 6(d) shows the approximately linear dependence of average ring crack spacing $\bar{d}$ and film thickness h, which can be understood by the collaborative fracture process of the film and substrate system [8].

During the indentation the tensile stress in the film is released by patterned cracks while the stretch energy is stored in the substrate. After the indenter is unloaded, the substrate begins to contract due to its elasticity, so the film would be under a compressive stress. The compressed film tilts up at the crack edge and the morphology of the buckle with a ridge crack appears. The results in Figs. 3 and 5 show the profile characteristics of the buckle. A theoretical work [41] has studied the feature of the straight buckle with a ridge crack and pointed out that the out-of-plane displacement solution $\zeta(x)$ of this buckle can be expressed by

$$\zeta(x) = \begin{cases} \delta_m\left[1 - \cos\pi p\left(\frac{x}{b} - 1\right)\right], & 0 < x \leqslant b \\ \delta_m\left[1 - \cos\pi p\left(\frac{x}{b} + 1\right)\right], & -b \leqslant x < 0, \end{cases} \tag{1}$$

where $\delta_m = F(p, \sigma_t)h/p\pi$ is the maximum buckle height with

$$F(p, \sigma_t) = \frac{\sin p\pi + \sqrt{\sin^2 p\pi + \frac{\pi^2}{3}\left(\frac{\sigma_t}{\sigma_c^E} - p^2\right)\left(1 - \frac{\sin 2p\pi}{2p\pi}\right)}}{1 - \frac{\sin 2p\pi}{2p\pi}}. \tag{2}$$

In this expression $1/2 \leqslant p \leqslant 1$ is defined as a dimensionless parameter to describe the effect of the crack on buckle height, where $p = 1/2$ indicates that the ridge crack is complete while $p = 1$ indicates that there is no crack. Here $b = w/2$ is defined as the half buckle width, σ_t is the compressive stress in the film, and $\sigma_c^E = \pi^2 E_f h^2/12(1 - v_f^2)b^2$ is the Euler buckling stress.

In our experiment the cracks in the film are complete and we assume $p = 1/2$; then the maximum buckle height becomes

$$\delta_m = \frac{2h}{\pi}\left[1 + \sqrt{1 + \frac{\pi^2}{3}\left(\frac{\sigma_t}{\sigma_c^E} - \frac{1}{4}\right)}\right]. \tag{3}$$

From this expression we can estimate the compressive stress in the film after the indenter is unloaded. The experimental results show that for the peak load $P = 10\,\mathrm{N}$ and film thickness $h = 30\,\mathrm{nm}$, the maximum height and buckle width of the cracked buckle are $\delta_m \approx 150\,\mathrm{nm}$ and $2b \approx 4.4\,\mu\mathrm{m}$, respectively. If we substitute δ_m, h, and b into Eq. (3) then the compressive stress can be obtained as $\sigma_t/\sigma_c^E \approx 14$. Furthermore, the analytical solution of the buckle profile with a ridge crack under such stress from Eq. (1) is plotted in Fig. 3(b). The comparison between the analytical solution and the experimental result shows good agreement. From Eq. (3) it is clear that the maximum buckle height is proportional to the film thickness $\delta_m \propto h$, which is also verified by the experimental measurement as shown in Fig. 5(g).

IV. CONCLUSION

In summary, the indentation-induced crack patterns in metal films on soft elastic PDMS substrates were described and discussed in detail. The indentation triggers the deformation of the film-substrate system, leading to the formation of multiple ring-shaped cracks. As the indentation load increases, the ring cracks first form near the indentation tip and then propagate outward step by step with a uniform spacing. They are not caused by the contact damage from the indenter but originate from the radial tensile stress due to the substrate deformation. The crack shape is thus insensitive to the indenter shape and indentation depth. However, the crack morphology is strongly dependent on the film thickness. The ring-shaped cracks are regular and possess a uniform spacing for thinner films, whereas they become very irregular as the film thickness increases. Furthermore, radial cracks become dominant for thicker films due to the competition between the radial stress on the film surface and circumferential stress at the film-substrate interface. The theoretical analysis showed that buckling structures tend to form near the cracks due to the induced compressive stress in the film after indentation, in good agreement with the experimental observations. The experimental and theoretical results presented in this paper will provide insight into the effect of indentation loading on the stress anisotropy and crack morphology. It is anticipated that more complex but ordered cracks can be achieved by tuning indenter shapes such as linear, circular, or elliptical arrays. The controllable formation of ordered cracks should be beneficial for a wide range of technological applications including patterned templates, micro- and nanofluidic devices, biological assays, ultrasensitive sensors, stretchable electronics, and surface engineering.

ACKNOWLEDGMENTS

This work was supported by the National Natural Science Foundation of China (Grants No. 91963123 and No. 11672285), the Strategic Priority Research Program of the Chinese Academy of Sciences (Grant No. XDB22040502), the Ten Thousand Talents Plan of Zhejiang Province (Grant No. 2018R52003), and the Fundamental Research Funds for the Provincial University of Zhejiang (Grant No. GK199900X022).

[1] L. Goehring, A. Nakahara, T. Dutta, S. Tarafdar, and S. Kitsunezaki, *Desiccation Cracks and Their Patterns: Formation and Modelling in Science and Nature* (Wiley, New York, 2015).

[2] X. Ma, J. Lowensohn, and J. C. Burton, Phys. Rev. E **99**, 012802 (2019).

[3] M. C. Milinkovitch, L. Manukyan, A. Debry, N. Di-Poï, S. Martin, D. Singh, D. Lambert, and M. Zwicker, Science **339**, 78 (2013).

[4] L. Goehring, R. Conroy, A. Akhter, W. J. Clegg, and A. F. Routh, Soft Matter **6**, 3562 (2010).

[5] Z. Neda, K.-t. Leung, L. Jozsa, and M. Ravasz, Phys. Rev. Lett. **88**, 095502 (2002).
[6] V. Lazarus and L. Pauchard, Soft Matter **7**, 2552 (2011).
[7] N. Wan, J. Xu, T. Lin, L. Xu, and K. Chen, Phys. Rev. B **80**, 014121 (2009).
[8] J. Marthelot, B. Roman, J. Bico, J. Teisseire, D. Dalmas, and F. Melo, Phys. Rev. Lett. **113**, 085502 (2014).
[9] K. H. Nam, I. H. Park, and S. H. Ko, Nature (London) **485**, 221 (2012).
[10] M. Kim, D. J. Kim, D. Ha, and T. Kim, Nanoscale **8**, 9461 (2016).
[11] Y. Han, Y. Liu, W. Wang, J. Leng, and P. Jin, Soft Matter **12**, 2708 (2016).
[12] A. Chortos, J. Lim, J. W. To, M. Vosgueritchian, T. J. Dusseault, T. H. Kim, S. Hwang, and Z. Bao, Adv. Mater. **26**, 4253 (2014).
[13] D. Kang, P. V. Pikhitsa, Y. W. Choi, C. Lee, S. S. Shin, L. Piao, B. Park, K. Y. Suh, T. Kim, and M. Choi, Nature (London) **516**, 222 (2014).
[14] B. C. Kim, C. Moraes, J. Huang, M. D. Thouless, and S. Takayama, Biomater. Sci. **2**, 288 (2014).
[15] D. Huh, K. L. Mills, X. Zhu, M. A. Burns, M. D. Thouless, and S. Takayama, Nat. Mater. **6**, 424 (2007).
[16] A. Yuse and M. Sano, Nature (London) **362**, 329 (1993).
[17] S. Yu, X. Liu, Y. Sun, H. Zhou, and P. Cai, Thin Solid Films **669**, 355 (2019).
[18] B. C. Kim, T. Matsuoka, C. Moraes, J. Huang, M. D. Thouless, and S. Takayama, Sci. Rep. **3**, 3027 (2013).
[19] B. C. Kim, C. Moraes, J. Huang, T. Matsuoka, M. D. Thouless, and S. Takayama, Small **10**, 4020 (2014).
[20] R. G. Elliman, M. Spooner, T. D. M. Dall, T. H. Kim, and N. H. Fletcher, Philos. Mag. **87**, 4893 (2007).
[21] B. E. Alaca, H. Sehitoglu, and T. Saif, Appl. Phys. Lett. **84**, 4669 (2004).
[22] M. Kim, D. Ha, and T. Kim, Nat. Commun. **6**, 6247 (2015).
[23] D. Kim, P. Makaram, and C. V. Thompson, Appl. Phys. Lett. **97**, 071902 (2010).
[24] S. Yu, Y. Sun, X. Zhang, C. Lu, H. Zhou, and Y. Ni, Phys. Rev. E **99**, 062802 (2019).
[25] N. P. Mitchell, V. Koning, V. Vitelli, and W. Irvine, Nat. Mater. **16**, 89 (2017).
[26] See Supplemental Material at http://link.aps.org/supplemental/10.1103/PhysRevE.102.022801 for details about the crack patterns in a variety of metal films on PDMS substrates with different film thicknesses and different peak loads taken by optical microscopy, atomic force microscopy, and scanning electron microscopy. Eight supplemental figures are provided.
[27] S. Yu, Y. Sun, Y. Ni, X. Zhang, and H. Zhou, ACS Appl. Mater. Interfaces **8**, 5706 (2016).
[28] K. Wu, J. Y. Zhang, G. Liu, P. Zhang, P. M. Cheng, J. Li, G. J. Zhang, and J. Sun, Acta Mater. **61**, 7889 (2013).
[29] T. X. Gao, Y. D. Sun, Y. F. Feng, and S. J. Yu, Philos. Mag. **96**, 2943 (2016).
[30] S. J. Yu, S. C. Li, Y. Ni, and H. Zhou, Acta Mater. **127**, 220 (2017).
[31] S. O. Kucheyev, A. V. Hamza, J. H. Satcher, and M. A. Worsley, Acta Mater. **57**, 3472 (2009).
[32] V. Keryvin, L. Charleux, R. Hin, J. P. Guin, and J. C. Sangleboeuf, Acta Mater. **129**, 492 (2017).
[33] K. Fu, Y. Yin, L. Chang, D. Shou, B. Zheng, and L. Ye, J. Phys. D **46**, 505314 (2013).
[34] J. Borc, K. Sangwal, I. Pritula, and E. Dolzhenkova, Mater. Sci. Eng. A **708**, 1 (2017).
[35] L. Goehring, W. J. Clegg, and A. F. Routh, Phys. Rev. Lett. **110**, 024301 (2013).
[36] M. R. Cho, J. H. Jung, M. key Seo, S. U. Cho, Y. D. Kim, J. H. Lee, Y. S. Kim, P. Kim, J. Hone, J. Ihm, and Y. D. Park, Sci. Rep. **7**, 43400 (2017).
[37] T. Khatun, M. D. Choudhury, T. Dutta, and S. Tarafdar, Phys. Rev. E **86**, 016114 (2012).
[38] H. Lama, V. R. Dugyala, M. G. Basavaraj, and D. K. Satapathy, Phys. Rev. E **94**, 012618 (2016).
[39] C. He, Z. Xie, Z. Guo, and H. Yao, J. Mech. Phys. Solids **83**, 19 (2015).
[40] M. Sakai, J. Zhang, and A. Matsuda, J. Mater. Res. **20**, 2173 (2005).
[41] S. C. Li, S. J. Yu, L. He, and Y. Ni, J. Mech. Phys. Solids **112**, 637 (2018).